


# Generation of Short Hard-X-Ray Pulses of Tailored Duration Using a Mössbauer Source

Guan-Ying Wang<sup>1</sup> and Wen-Te Liao<sup>1,2,\*</sup>

<sup>1</sup>*Department of Physics, National Central University, Taoyuan City 32001, Taiwan*

<sup>2</sup>*Max Planck Institute for Nuclear Physics, Saupfercheckweg 1, 69117 Heidelberg, Germany*

 (Received 15 September 2017; revised manuscript received 25 April 2018; published 6 July 2018)

We theoretically investigate a scheme for the generation of single hard-x-ray pulses of controllable duration in the range of 1–100 ns from a radioactive Mössbauer source. The scheme uses a magnetically perturbed  $^{57}\text{FeBO}_3$  crystal illuminated with recoilless 14.4-keV photons from a  $^{57}\text{Co}$  radioisotope nuclide. Such a compact x-ray source is useful for the extension of quantum optics to the 10-keV energy scale, which has been in the spotlight in recent years. So far, experimental achievements have mostly been attained in synchrotron radiation facilities. However, the use of tabletop and portable hard-x-ray sources for time-resolved measurements and for implementing coherent control over nuclear quantum-optics systems has still been limited. The availability of compact hard-x-ray sources may become the engine for the application of quantum-information schemes down to the subatomic scale. We demonstrate that the present method is versatile and provides an economic solution, utilizing a Mössbauer source, to perform time-resolved nuclear scattering, to produce suitable pulses for photon storage, and to flexibly generate x-ray single-photon entanglement.

DOI: [10.1103/PhysRevApplied.10.014003](https://doi.org/10.1103/PhysRevApplied.10.014003)

## I. INTRODUCTION

X-ray quantum optics [1] opens up a completely new angstrom-wavelength regime for the study of light-matter interactions. Recently, many remarkable experiments [2–14] have been achieved with synchrotron radiation (SR) or x-ray free-electron lasers (XFELs). Many new systems [15–28] based on x-ray facilities have also been theoretically investigated. One of reasons that SR becomes superior to a Mössbauer source—namely, a radioisotope—is the very short time structure of SR. When utilizing SR to excite nuclear transitions, its picosecond pulse duration allows for the discrimination of resonantly scattered photons from both the background radiation of SR and instantaneous nonresonant charge scattering in the time domain [29,30]. This method, a remarkable suggestion by Ruby [30], has led to great success in the field of nuclear-condensed-matter physics [29] and forms the basis for many nuclear schemes in x-ray quantum optics [2,6,8,11–14,16,18,20]. Instead of a total photon number per pulse, a key x-ray parameter to drive nuclear transitions is the number of resonant photons per pulse. A typical SR pulse contains less than one resonant photon on average [2,6,8,11–14,16,18,20]. It is therefore of great interest to find methods of producing short hard-x-ray pulses with a suitable temporal profile from typical Mössbauer sources

[31], since a radioisotope naturally delivers resonant photons and is portable and more affordable than an x-ray facility. Moreover, for many applications, such as quantum information [16,23,25,26,31], it is more convenient to use a compact x-ray source such as a radioisotope than a SR facility. The unperturbed time structure of the emitted x-ray pulses from a typical Mössbauer source, however, may not be suitable for a variety of purposes. In a photon storage scheme [23], for example, a moderate duration for the pulse to be stored is preferable, i.e., shorter than the coherence time of a memory medium but longer than the inverse of the memory bandwidth. The generation of such single hard-x-ray pulses is not trivial using the available schemes [23,31]. It is therefore important to develop methods to generate x-ray wave packets of a mission-oriented duration from a conventional Mössbauer source [19,23,31]. Here, we investigate an all-field scheme using a magnetically perturbed  $^{57}\text{FeBO}_3$  crystal [2,32,33] to generate short single hard-x-ray pulses of adjustable duration in the 1–100-ns range. The present tabletop scheme can be useful for time-resolved measurements, x-ray quantum optics, and even probing the gravitational deflection of x rays in any laboratory [34].

## II. SYSTEM

Figure 1 illustrates the setup, which is a variation of the experimental arrangements suggested and applied in Refs. [35,36] for other subjects. In a Mössbauer source,

\*wente.liao@g.ncu.edu.tw

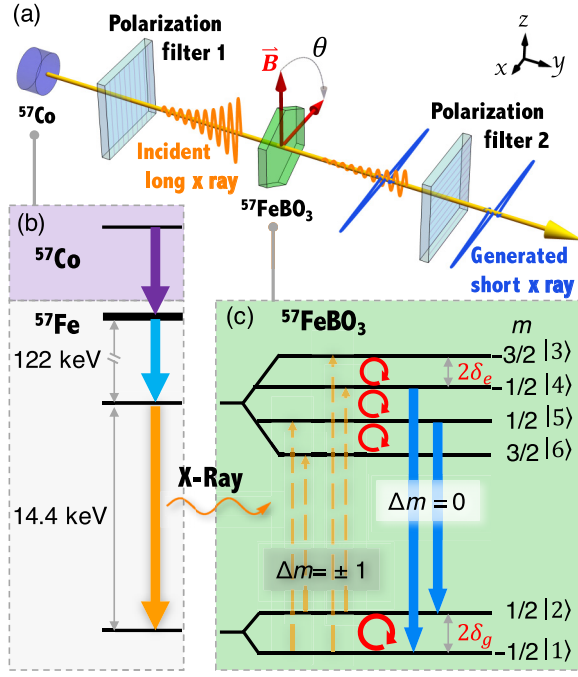


FIG. 1. (a) A vertically polarized (along the  $z$  axis) x ray of 14.4 keV (orange wavy curve) from a  $^{57}\text{Co}$  Mössbauer source impinges on a  $^{57}\text{FeBO}_3$  crystal (green hexagon). A horizontally polarized (along the  $x$  axis) x ray (blue sharp curve) is generated when properly switching the magnetization of a  $^{57}\text{FeBO}_3$  crystal by an external magnetic field  $\vec{B}$  (red rotating arrows). (b) In a radioisotope source, the  $^{57}\text{Co}$  nuclide becomes  $^{57}\text{Fe}$  via electron capture, and then the decayed  $^{57}\text{Fe}$  nucleus emits  $\gamma$  rays of 122 keV and subsequently hard x rays of 14.4 keV polarized by polarization filter 1. (c) Orange thin-dashed upward arrows indicate four possible  $\Delta m = \pm 1$  nuclear  $M1$  transitions of  $^{57}\text{Fe}$  that could be excited by the vertically polarized x rays. By dynamically switching the angle  $\theta$  between the  $z$  axis and  $\vec{B}$ , the hyperfine splitting  $2\delta_g$  ( $2\delta_e$ ) among the ground (excited) states is modulated. Due to the magnetic switching, the emission of x rays with horizontal polarization (two blue thick downward arrows) via two  $\Delta m = 0$  transitions is controllable.

the radioactive  $^{57}\text{Co}$  nuclei become excited  $^{57}\text{Fe}$  nuclei via electron capture. The excited  $^{57}\text{Fe}$  nuclei then experience a cascade decay and emit in turn 122- and 14.4-keV photons. To observe single-photon events in a typical Mössbauer experiment, the detection of the former triggers the time sequence of probing a nuclear target of interest using the latter [31]. A recoilless and vertically polarized [33,37] 14.4-keV x ray, of duration 141 ns, from a  $^{57}\text{Co}$  radioisotope source [see Fig. 1(b)] impinges on an isotopically enriched  $^{57}\text{FeBO}_3$  crystal. We invoke the elegant magnetic property of an iron borate  $^{57}\text{FeBO}_3$  crystal, whose strong magnetization can be rotated via an external weak magnetic field  $\vec{B}$  of a few gauss in  $<1$  ns [38]. A recent study with femtosecond laser pulses suggests even faster control over iron borate [39]. This property allows for fast

switching of the internal magnetic hyperfine field at the  $^{57}\text{Fe}$  nuclei, and therefore renders possible control over the dynamics of the nuclear excitations [2,16,33], e.g., nanosecond stepwise modulation of Mössbauer radiation is realized [32]. We emphasize that our work aims at the generation of a very short pulse of controllable duration in the range of 1–100 ns. Reference [32] focused on the production of a very long ( $>400$  ns) rectangular pulse with a sharp edge. Neither any motivation nor any mechanism is shared by two works. The  $^{57}\text{Fe}$  nuclear-level scheme with hyperfine splitting of the ground and excited states of, respectively, spins  $I_g = 1/2$  and  $I_e = 3/2$  is illustrated in Fig. 1(c). When choosing the  $z$  axis as the quantization axis, the vertically polarized x ray (VPX) is treated as a superposition of right-circularly-polarized x rays (RCPXs) and left-circularly-polarized x rays (LCPXs). Therefore, the VPX drives  $\Delta m = \pm 1$  nuclear magnetic dipole ( $M1$ ) transitions of  $^{57}\text{Fe}$  in the crystal [40]. In view of the fact that the hyperfine splitting is greater than the linewidth, an incident x ray can resonantly drive only one transition to which it is tuned. Alternatively, with higher resonant thickness of a target, each transition can also be driven off-resonantly. The projections of the crystal magnetization in the quantization axis cause hyperfine splitting proportional to  $\cos\theta$  and simultaneously Larmor precession about the  $x$  axis, with frequencies proportional to  $\sin\theta$ . The Larmor precession leads to cross talk between the orthogonal polarizations of a single photon. One can therefore switch the crystal magnetization back and forth to create a time window allowing for transient cross talk, which transforms a temporal slice of a long pulse of a specific polarization into another polarization, which was not studied in Ref. [32]. In what follows, we will invoke the above cross-talk dynamics to control the duration of produced x-ray pulses.

### III. MODEL

Coupling between nuclei and x rays is described by the optical Bloch equation (OBE) in the perturbation region [41], i.e., where the Rabi frequency is much less than the spontaneous decay rate (see definition below) [19]. The OBE, which is numerically solved by using the Runge-Kutta fourth-order method [42], reads as follows:

$$\begin{aligned} \partial_t \hat{\rho} &= \frac{1}{i\hbar} [\hat{H}, \hat{\rho}] + \mathcal{L}\rho, \\ \hat{H} &= \hat{H}_i + \hat{H}_h^z + \frac{\partial\theta}{\partial t} \hat{J}_y, \\ \frac{1}{c} \partial_t \Omega_R + \partial_y \Omega_R &= i\eta(a_{51}\rho_{51} + a_{62}\rho_{62}), \\ \frac{1}{c} \partial_t \Omega_H + \partial_y \Omega_H &= i\eta(a_{41}\rho_{41} + a_{52}\rho_{52}), \\ \frac{1}{c} \partial_t \Omega_L + \partial_y \Omega_L &= i\eta(a_{31}\rho_{31} + a_{42}\rho_{42}), \end{aligned} \quad (1)$$

where  $\eta = 6\Gamma\alpha/L$ ,  $\alpha$  is the resonant thickness,  $\Gamma = 1/141 \times 10^9 \text{ s}^{-1}$  is the radioactive decay rate of the nuclear excited state, and  $L$  is the crystal thickness.  $\hat{\rho}$  is the density matrix for the state vector  $\sum_{i=1}^6 A_i|i\rangle$  of the six-level  $^{57}\text{Fe}$  nuclei, and each coherence  $\rho_{ij} = A_i A_j^*$ .  $\hat{H}_i$  is the interaction Hamiltonian describing the nucleus–x-ray coupling. For general cases of continuous magnetic switching, it is convenient to fix the quantization axis along the  $z$  axis and then rotate the hyperfine splitting Hamiltonian at each  $\theta$  back onto the  $z$  axis.  $\hat{H}_h^z$  therefore depicts the rotated hyperfine Hamiltonian. The additional  $(\partial\theta/\partial t)\hat{J}_y$  term denotes the rotational energy introduced by the magnetic switching. The explicit form of all Hamiltonian matrices is given in Appendix A.  $\hat{J}_y$  is the  $y$  component of the angular momentum operator [43], and the  $\partial\theta/\partial t$  results from the time-dependent rotational matrix (for a detailed derivation, see Appendix B).  $\mathcal{L}\rho$  describes the radioactive decay of the excited states, namely, the losses in the  $4\pi$  solid angle. The x-ray loss due to  $K$ -shell photoionization is negligible because the nuclear resonance absorption cross section  $\sigma_0$  is much larger than the total electronic absorption cross section  $\sigma_{\text{ph}}$ , namely,  $\sigma_0/\sigma_{\text{ph}} \sim 429$  at 14.4 keV [29].  $\Omega_R(t, y)$ ,  $\Omega_L(t, y)$ , and  $\Omega_H(t, y)$  are the Rabi frequencies of the RCPX, the LCPX, and the horizontally polarized x ray (HPX) (parallel to the  $x$  axis in Fig. 1(a)), respectively. Each wave equation describes the forward propagation of x rays of different polarizations.  $a_{31} = 1$ ,  $a_{41} = \sqrt{2/3}$ ,  $a_{51} = \sqrt{1/3}$ ,  $a_{42} = \sqrt{1/3}$ ,  $a_{52} = \sqrt{2/3}$ , and  $a_{62} = 1$  are the Clebsch-Gordan coefficients of the corresponding transitions. A comparison will be drawn between the case with a fixed  $\vec{B}$  and that with a switched  $\vec{B}$ .

#### IV. RESULTS AND DISCUSSION

Figure 2 demonstrates the effects of magnetic switching. The gray dashed lines in Fig. 2 show the input x-ray intensity from the  $^{57}\text{Co}$  nuclide. For both cases, the inputs are  $\Omega_R(t, 0) = \Omega_L(t, 0) = \Omega_0 e^{-\Gamma t/2}$ . Note that, in the perturbation region, neither the time structure of the output nor the output to input ratio is changed by the value of  $\Omega_0$ . Therefore,  $\Omega_0$  becomes a normalization factor. For convenience, we set  $\Omega_0 = 1$ , and then all results in what follows are normalized by the maximum intensity of an incident pulse. In our calculation, the initial moment  $t = 0$  is determined by a measurement of 122 keV photons emitted by the decay process illustrated by Fig. 1(b). The initial conditions are given by the fact that all of the initial x-ray fields are zero and that there is initial zero coherence  $\rho_{ij}(0, y) = 0$  for  $i \neq j$ . Due to very weak input x rays, the variation of all populations is negligible in the perturbation region, i.e.,  $\rho_{11}(t, y) = \rho_{22}(t, y) = 1/2$ ,  $\rho_{ii}(t, y) = 0$  for  $i > 2$ . The  $^{57}\text{FeBO}_3$  parameters used are  $\alpha = 30$ , with the hyperfine splitting of ground states  $\delta_g = 12.63\Gamma$  and

that of excited states  $\delta_e = 7.37\Gamma$ . We first show the output x-ray intensity for a fixed  $\vec{B}$  in Fig. 2(a), where the input and output polarizations are the same (termed the unperturbed signal). The output RCPX  $|\Omega_R(t, L)|^2$  (red solid line) and LCPX  $|\Omega_L(t, L)|^2$  (not shown) are identical and result from zero x-ray detuning and dispersion. Figures 2(b)–2(d) illustrate an example in which we continuously switch the external  $\vec{B}$ . The time sequence of the rotated magnetic field is given by Fig. 2(b). Two continuous but opposite  $90^\circ$  magnetic switchings are applied to a  $^{57}\text{FeBO}_3$  crystal, and their switching paths are depicted by two sketches. The first clockwise switching from  $0^\circ$  to  $90^\circ$  is implemented at around 110 ns, and then the  $\vec{B}$  field remains at  $90^\circ$  for 200 ns. Subsequently, the second counterclockwise rotation switches the magnetization back to its initial orientation at around 310 ns. As demonstrated in Figs. 2(c) and 2(d), the above magnetic switching transfers a temporal fraction of the RCPX, namely, the missing part during  $110 \text{ ns} < t < 310 \text{ ns}$  in Fig. 2(c), to the HPX. Because both RCPXs and LCPXs contribute equal amounts of energy to the HPX, the HPX intensity is double that of the transferred part in the unperturbed RCPX.

Given the capability of transferring photons from one polarization to another by the above scheme, in Fig. 3 we illustrate how to use the method to generate short hard-x-ray pulses of tailored pulse durations. Figure 3(a) depicts a sequence of switching  $\vec{B}$  back and forth between  $0^\circ$  and  $90^\circ$  at three different rates. As one can see in Fig. 3(b), the magnetic switching cuts three splits of corresponding widths in the perturbed RCPX signal (indicated by the vertical green arrows). Our calculation shows that an identical situation also happens in the LCPX. Figure 3(c) illustrates that the missing fractions of the circularly polarized x rays are transferred to the HPXs as individual pulses having durations of, in turn, 1.3, 10, and 20 ns, depending on how fast  $\vec{B}$  is rotated. With a given resonant thickness and hyperfine splitting of a  $^{57}\text{FeBO}_3$  crystal, the peak intensity and peak position of a generated single pulse can be adjusted by the switching process. For example, in Fig. 3(c), the reason that the shortest pulse has the highest intensity is because the switched  $\vec{B}$  reaches the angle of  $90^\circ$  at the instant when the unperturbed  $|\Omega_R(t, L)|^2$  is at a maximum. The slight asymmetry of each pulse represents the ripples of the unperturbed circularly polarized x rays. Also, the speed of the switching controls the generated pulse durations, which highlights the flexibility of the method. It is worth mentioning that a successful magnetic slicing of x rays does not rely on precise knowledge of the moment of switching. Without a coincidence technique, the result would become the average over many possible upcoming VPX wave packets, but the duration of a generated HPX short pulse would remain unchanged.

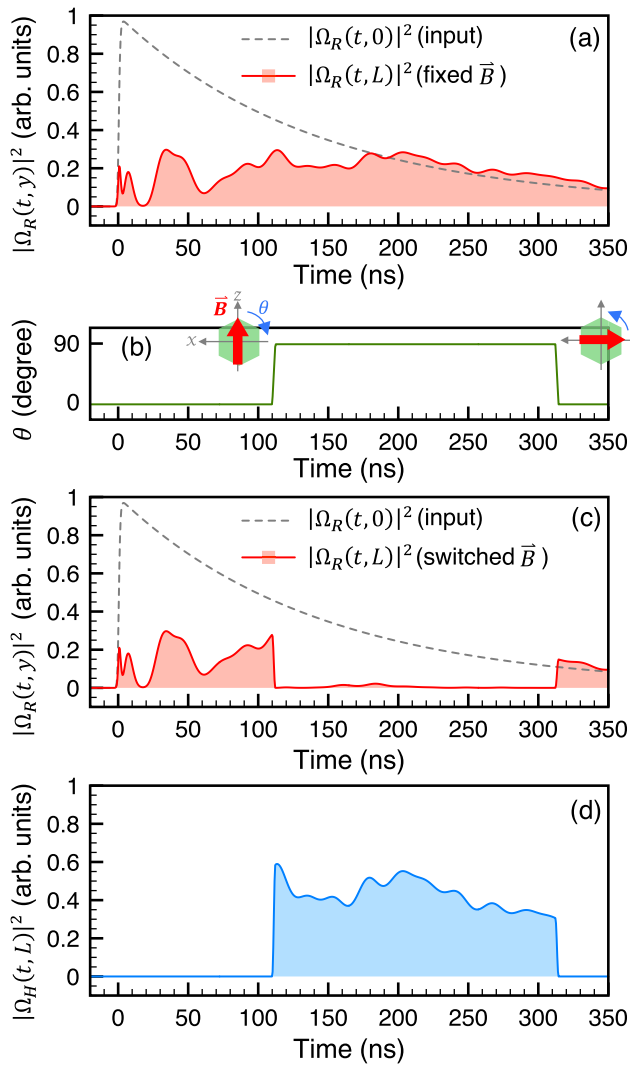


FIG. 2. Without magnetic switching (a) (fixed  $\vec{B}$ ), the red solid line depicts the intensity of the scattered right-circularly-polarized x ray  $|\Omega_R(t, L)|^2$ . The gray dashed line depicts the input  $|\Omega_R(t, 0)|^2$ . With the magnetic switching, whose time sequence is demonstrated in panel (b), the magnetic rotation transfers a temporal fraction of (c) the right-circularly-polarized x ray to (d) the horizontally polarized component. Two sketches in panel (b) visualize  $90^\circ$  magnetic rotations applied to a  $^{57}\text{FeBO}_3$  crystal at around 110 and 310 ns. Red arrows represent the applied magnetic field, the blue curved arrows show the switching paths, and the green hexagons illustrate the  $^{57}\text{FeBO}_3$  crystal. All results are normalized by the maximum value of  $|\Omega_R(t, 0)|^2$ .

### V. THREE TYPES OF MAGNETIC SWITCHING

We discuss three types of magnetic switching, as illustrated in Fig. 4(a). Type A switching (the green dashed-dotted line) illustrates two abrupt but opposite  $90^\circ$  switchings at 110 ns, and subsequently at 116 ns. Type B (the blue solid line) depicts a continuous rotation from  $0^\circ$  to  $180^\circ$ . Type C (the red dashed line) is the same kind of switching as used in Fig. 3. The generated single pulses  $|\Omega_H(t, L)|^2$

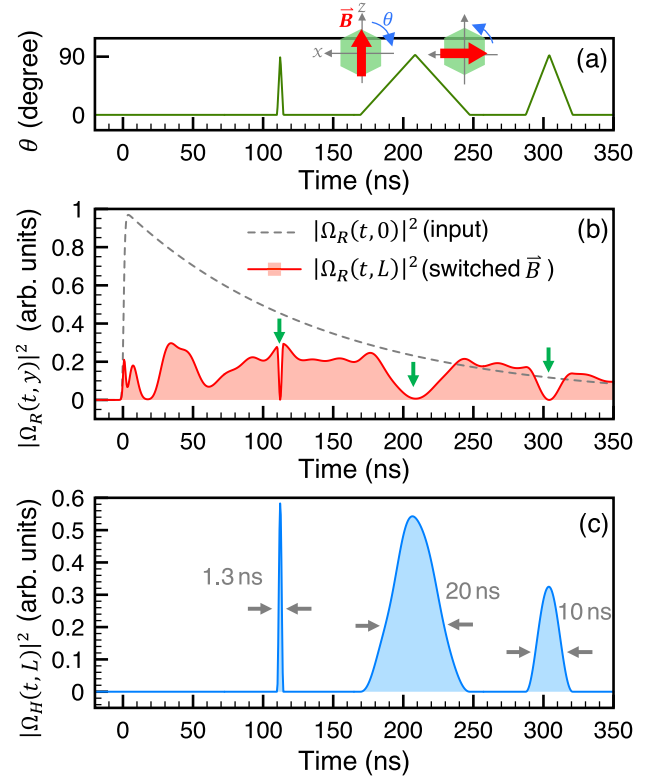


FIG. 3. Panel (a) depicts three magnetic rotations at different rates applied to a  $^{57}\text{FeBO}_3$  crystal. All single pulses are generated by two opposite  $90^\circ$  rotations of  $\vec{B}$ . Two sketches visualize the  $90^\circ$  magnetic rotations during 170 and 250 ns. Panel (b) illustrates the input (gray dashed line) and output (red solid line) right-circularly-polarized x rays. The three vertical green arrows indicate three temporal splits cut by magnetic switching at different rates. Panel (c) demonstrates the generation of three horizontally polarized single-x-ray pulses with durations of 1.3, 20, and 10 ns. All results are normalized by the maximum value of  $|\Omega_R(t, 0)|^2$ .

are shown in Fig. 4(b) on a logarithmic scale. The peak intensity of the pulse generated by type A switching (the green dashed-dotted line) is greater than that of the input x rays, but the main pulse, which appears before 120 ns, is always followed by other small oscillating signals. The single pulse produced by type B switching (the blue solid line) and that by type C (the red dashed line) are almost identical on a linear scale. However, on a logarithmic scale, the main distinction between the various schemes can be observed. Each generated single pulse is followed by quantum beat signals [44], and the ratios between the peak intensity and the beating signals are 10,  $10^4$ , and  $10^6$  for types A, B, and C, respectively. This suggests that short hard-x-ray pulses from type B and type C schemes are useful for time-resolved x-ray experiments, e.g., nuclear forward scattering (NFS).

The Larmor spin precession among hyperfine sub-levels actually affects the time structure of the  $\Delta m = 0$

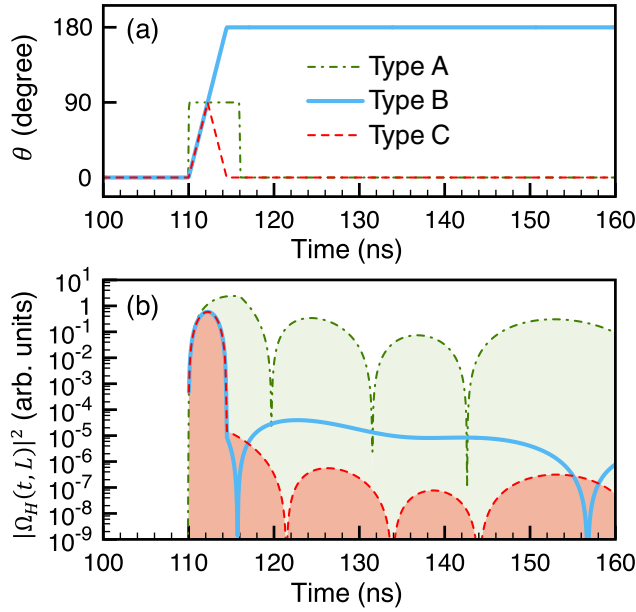


FIG. 4. Panel (a) demonstrates three types of magnetic switching. Type A (the green dashed-dotted line) depicts two prompt but opposite  $90^\circ$  rotations at 110 and 116 ns, type B (the blue solid line) illustrates a continuous  $180^\circ$  switching, and type C (the red dashed line) depicts two continuous but opposite  $90^\circ$  rotations. Panels (a) and (b) share the same legend. The correspondingly generated single short x-ray pulses via three types of switching are illustrated in panel (b) on a logarithmic scale. All results are normalized by the maximum value of  $|\Omega_R(t, 0)|^2$ .

emissions. If the Larmor precession did not happen, the transformation back and forth between the  $\Delta m = \pm 1$  and  $\Delta m = 0$  coherences would be perfect and then the duration of the generated pulse would only depend on how long the magnetization stayed at  $90^\circ$ . However, this is not the case. Once the magnetization has stayed at  $90^\circ$  for too long, as in type A switching, due to Larmor precession, the  $\Delta m = 0$  emission will not be suppressed after switching back. Type A switching therefore gives longer pulses. To overcome this problem, we therefore use  $\pi/2$ -angle back-and-forth (type C) and  $\pi$  switching (type B) of the magnetic field to minimize the effect of Larmor precession; in other words, before the nuclei have experienced too much spin precession, the magnetization has already left the  $\pi/2$  direction. This is the reason why  $\pi/2$ -angle back-and-forth and  $\pi$  switching produce the same single leading pulse in our Fig. 4(b).

## VI. ESTIMATION OF PHOTON COUNTING RATES

We estimate the vertically polarized photon counting rate  $\chi_1$  at the first crystal by means of the following formula in spherical coordinates:

$$\chi_1 = A \frac{\Theta}{4\pi} P_V, \quad (2)$$

$$\Theta = \int_0^{2\pi} \int_0^{\tan^{-1}(w/2D)} \sin \vartheta d\vartheta d\phi. \quad (3)$$

Here, the activity of the 200 mCi  $^{57}\text{Co}$  source is  $A = 7.4 \times 10^9$  counts/s. When  $\gamma$  decay happens equally in the total  $4\pi$  solid angle, one has to calculate the fraction of photons emitted in the forward direction within a small solid angle  $\Theta$ . As depicted in Fig. 5, assuming that the distance between a radioisotope source and the first crystal is  $D = 20$  cm and the width of the first  $^{57}\text{FeBO}_3$  crystal is  $w = 5$  mm, these parameters result in a solid angle of  $5 \times 10^{-4}$  sr in the forward direction. In order to calculate the probability  $P_V$  of the emission of vertically polarized photons by a  $^{57}\text{Co}$  source, one can choose the  $x$  axis as the quantization axis and then look at the  $\Delta m = 0$  transitions. Analysis of the Clebsch-Gordan coefficients shows that  $P_V = (a_{41}^2 + a_{52}^2)/(a_{41}^2 + a_{52}^2 + a_{51}^2 + a_{62}^2 + a_{31}^2 + a_{42}^2) = \frac{1}{3}$ . With the above-noted parameters,  $\chi_1 = 96\,343$  counts/s is obtained. The production rate  $\chi_2$  of horizontally polarized photons at the second crystal can be estimated by

$$\chi_2 = \chi_1 \frac{\int_0^\infty |\Omega_H(t, L)|^2 dt}{2 \int_0^\infty e^{-\Gamma t} dt}. \quad (4)$$

The denominator represents the total temporal area of the incident VPX pulse, and the numerator denotes that of the generated HPX pulse. The area ratio in Eq. (4) gives the conversion efficiency from vertically to horizontally polarized x rays. For three single pulses in Fig. 3(c), the area ratios are, respectively, 0.0045, 0.069, and 0.019, and so the HPX photon production rates are, in turn, estimated to be 430, 6600, and 1800  $\text{s}^{-1}$ . The area ratio of the 1.3-ns pulse in Fig. 3(c) is tripled to 0.013 by using a thicker  $^{57}\text{FeBO}_3$  crystal of  $\alpha = 100$ ,  $\delta_e = 31\Gamma$ , and  $\delta_g = 53\Gamma$ . The converted horizontally polarized x rays are demonstrated

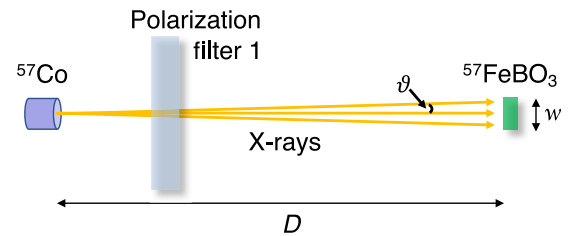


FIG. 5. An illustration for the estimation of the photon counting rates. The distance  $D$  between a radioisotope source and the  $^{57}\text{FeBO}_3$  crystal and the crystal width  $w$  are used to calculate the solid angle.  $\vartheta$  denotes the polar angle in spherical coordinates.

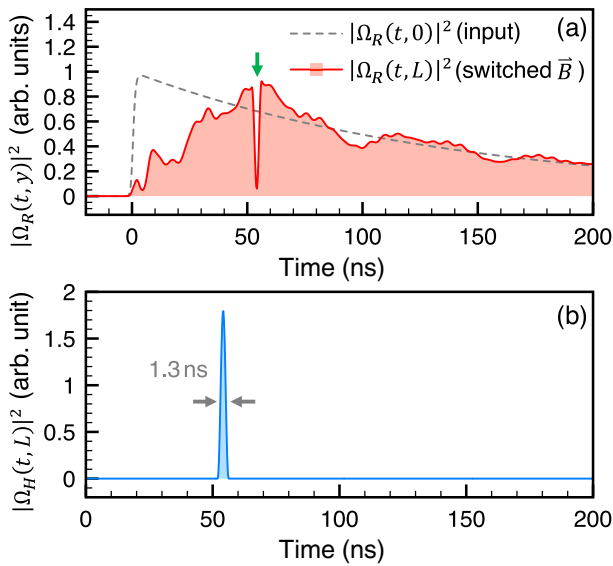


FIG. 6. As a comparison with Fig. 3, the photon counting rates of a horizontally polarized x ray at the second target are tripled by using a thicker  $^{57}\text{FeBO}_3$  crystal of  $\alpha = 100$ ,  $\delta_e = 31\Gamma$ , and  $\delta_g = 53\Gamma$ . All results are normalized by the maximum value of  $|\Omega_R(t, 0)|^2$ .

in Fig. 6(b). The present scheme is a sort of magnetic slicing, and so one can slice different parts of the unperturbed vertically polarized output pulse. Performing magnetic switching at maximal values will optimize the transformation efficiency, e.g., at  $t = 110$  ns in Fig. 3 and at  $t = 54$  ns in Fig. 6. Without any special modulation, one would expect that the maximum conversion efficiency of a 1 ns pulse would be about 0.7% by simple pulse area estimation, namely,  $(I_0 \times 1 \text{ ns}) / \int_0^\infty I_0 e^{-\Gamma t} dt = 0.007$ , assuming a sliced square pulse of duration 1 ns and amplitude  $I_0$ . A higher efficiency of about 1% in Fig. 6 is achieved by pulse propagation, which provides better compression of the incident pulse and, critically, determines the conversion efficiency. The above HPX counting rates are given by repeating the magnetic switching every few hundred nanoseconds, i.e., by the duration of the input pulse. For applications of probing dynamics over longer time scales or with lower triggering efficiencies, successful switching may happen every 0.01 ms and still produce reasonable numbers of resonant photons per second (the above HPX rates divided by a factor of 50). A 100-kHz repetition rate for the switching should also cause much less heating (by  $\ll 15$  K) of the crystal than a MHz repetition rate [32,33,38]. Also, during switching, magnetoelastic oscillations with a frequency of few MHz will cause modulations on longer x-ray pulses [32,33,38]. Solutions to suppress the intensity of magnetoelastic oscillations have been demonstrated, e.g., by using several thin crystals instead of a thick one [32].

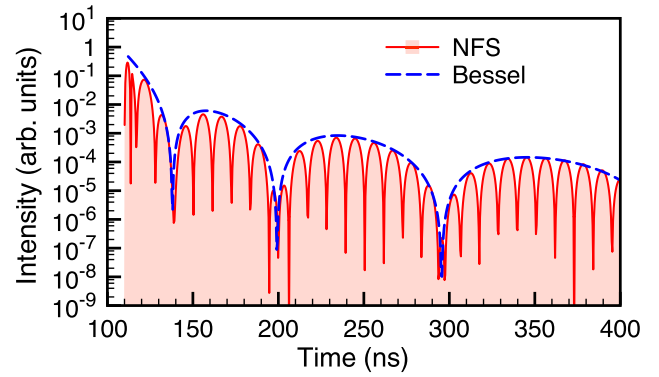


FIG. 7. The generated leftmost single pulse of duration of 1.3 ns in Fig. 3(c) is used to probe a downstream nuclear target with nuclear forward scattering. Red solid line illustrates the NFS signal and the blue dashed line shows the typical Bessel fitting.

## VII. CONCLUSION

We would like to emphasize that the present scheme is a solution for some potential applications that have so far only been considered suitable for SR facilities. (1) Figures 2 and 3 demonstrate the flexible generation of x-ray single-photon entanglement subject to polarization [16,17], namely, the single-photon wave packet (Figs. 2(c), 2(d), 3(b), and 3(c)) is described by  $|\psi\rangle = |1\rangle_V|0\rangle_H + |0\rangle_V|1\rangle_H$ . Our calculation shows that a successful production of entanglement via the present scheme is not sensitive to the moment of switching [16]. It therefore allows us to freely choose when to turn on the polarization transducer, as demonstrated in Figs. 2 and 3. (2) The present scheme makes tailored pulse duration available for a range of uses. It is not trivial to produce an x-ray pulse with a mission-oriented duration, e.g., 28 ns for x-ray photon storage [23]. As depicted in Fig. 3, the present scheme offers a solution for such a purpose by changing the switching rate. Based on our calculations, a hard-x-ray pulse of a duration in the range of 1–100 ns can be produced by the present scheme. (3) The scheme sets out a possible use for time-resolved measurements. We utilize the produced HPX of duration 1.3 ns, i.e., the leftmost peak in Fig. 3(c), as the incident field for the second  $^{57}\text{Fe}$ -enriched target to be probed by nuclear forward scattering. Figure 7 depicts the scattered x ray of the second target, whose parameters are resonant depth  $\alpha_2 = 20$ ,  $\delta_g = 25.26\Gamma$ , and  $\delta_e = 14.74\Gamma$ . The envelope (the blue dashed line) of the NFS signal is the so-called dynamical beat [45] and is described by  $[(\alpha_2/\sqrt{\alpha_2\Gamma t})J_1(2\sqrt{\alpha_2\Gamma t})]^2 e^{-\Gamma t}$ , where  $J_1$  is a Bessel function of the first kind [45]. The modulated Mössbauer source allows us to temporally resolve the quantum beat [45] caused by the hyperfine splitting of the sample, which has so far only been possible with SR [46–48].

In conclusion, we have theoretically investigated a method using a  $^{57}\text{Co}$  x-ray source and a magnetically

perturbed  $^{57}\text{FeBO}_3$  crystal as a polarization transducer to generate single hard-x-ray pulses of tailored pulse durations in the range of 1–100 ns. We expect that the present system will become an economic tool, complementary to other ultrashort hard-x-ray sources, for a variety of purposes. Also, the adjustable pulse duration given by the present scheme offers the flexible generation of time-bin qubits [31], arbitrary pulse trains, and proper x-ray pulses for photon storage [23].

### ACKNOWLEDGMENTS

We thank S. M. Cavaletto, K. Heeg, J. Gunst, S. Bragin, A. Pálffy, J. Evers, and B. Nickerson for carefully reading the manuscript and for fruitful discussions. G.-Y. W. and W.-T. L. are supported by the Ministry of Science and Technology, Taiwan (Grant No. MOST 105-2112-M-008-001-MY3). W.-T. L. is also supported by the National Center for Theoretical Sciences, Taiwan.

### APPENDIX A: OPTICAL BLOCH EQUATION FOR THE CASE OF A FIXED MAGNETIC FIELD

The system of a fixed magnetic field under study is described by the optical Bloch equation (OBE) [19,41]:

$$\partial_t \hat{\rho} = \frac{1}{i\hbar} [\hat{H}, \hat{\rho}] + \mathcal{L}\rho,$$

$$\hat{H} = \hat{H}_i + \hat{H}_h,$$

$$\frac{1}{c} \partial_t \Omega_R + \partial_y \Omega_R = i \frac{6\Gamma\alpha}{L} (a_{51}\rho_{51} + a_{62}\rho_{62}), \quad (\text{A1})$$

$$\frac{1}{c} \partial_t \Omega_H + \partial_y \Omega_H = i \frac{6\Gamma\alpha}{L} (a_{41}\rho_{41} + a_{52}\rho_{52}),$$

$$\frac{1}{c} \partial_t \Omega_L + \partial_y \Omega_L = i \frac{6\Gamma\alpha}{L} (a_{31}\rho_{31} + a_{42}\rho_{42}),$$

where  $\alpha$  is the resonant thickness,  $\hat{\rho}$  is the density matrix for the state vector  $\sum_{i=1}^6 A_i |i\rangle$  of the six-level  $^{57}\text{Fe}$  nuclei, and each coherence  $\rho_{ij} = A_i A_j^*$ ;

$$\hat{H}_i = -\frac{\hbar}{2} \begin{pmatrix} 0 & 0 & a_{13}\Omega_L^* & a_{14}\Omega_H^* & a_{15}\Omega_R^* & 0 \\ 0 & 0 & 0 & a_{24}\Omega_L^* & a_{25}\Omega_H^* & a_{26}\Omega_R^* \\ a_{31}\Omega_L & 0 & -2\Delta_L 0 & 0 & 0 & 0 \\ a_{41}\Omega_H & a_{42}\Omega_L & 0 & -2(\Delta_L + \Delta_H) & 0 & 0 \\ a_{51}\Omega_R & a_{52}\Omega_H & 0 & 0 & -2(\Delta_H + \Delta_R) & 0 \\ 0 & a_{62}\Omega_R & 0 & 0 & 0 & -2\Delta_R \end{pmatrix} \quad (\text{A2})$$

is the interaction Hamiltonian describing the nucleus–x-ray interaction with the Rabi frequencies  $\Omega_R$  of the right-circularly-polarized field,  $\Omega_H$  of the horizontally polarized field, and  $\Omega_L$  of the left-circularly-polarized field.  $a_{31} = 1$ ,  $a_{41} = \sqrt{\frac{2}{3}}$ ,  $a_{51} = \sqrt{\frac{1}{3}}$ ,  $a_{42} = \sqrt{\frac{1}{3}}$ ,  $a_{52} = \sqrt{\frac{2}{3}}$ , and  $a_{62} = 1$  are the Clebsch-Gordan coefficients of the corresponding transitions. All x-ray detunings are zero, where  $\Delta_R$  is the detuning of the right-circularly-polarized field,  $\Delta_H$  is that of the horizontally polarized field, and  $\Delta_L$  is that of the

left-circularly-polarized field;

$$\hat{H}_h = \hbar \begin{pmatrix} -\delta_g & 0 & 0 & 0 & 0 & 0 \\ 0 & \delta_g & 0 & 0 & 0 & 0 \\ 0 & 0 & 3\delta_e & 0 & 0 & 0 \\ 0 & 0 & 0 & \delta_e & 0 & 0 \\ 0 & 0 & 0 & 0 & -\delta_e & 0 \\ 0 & 0 & 0 & 0 & 0 & -3\delta_e \end{pmatrix}$$

depicts the hyperfine splitting;

$$\mathcal{L}\rho = \frac{\Gamma}{2} \begin{pmatrix} 2(a_{31}^2\rho_{33} + a_{41}^2\rho_{44} + a_{51}^2\rho_{55}) & 0 & -\rho_{13} & -\rho_{14} & -\rho_{15} & -\rho_{16} \\ 0 & 2(a_{42}^2\rho_{44} + a_{52}^2\rho_{55} + a_{62}^2\rho_{66}) & -\rho_{23} & -\rho_{24} & -\rho_{25} & -\rho_{26} \\ -\rho_{31} & -\rho_{32} & -2\rho_{33} & -2\rho_{34} & -2\rho_{35} & -2\rho_{36} \\ -\rho_{41} & -\rho_{42} & -2\rho_{43} & -2\rho_{44} & -2\rho_{46} & -2\rho_{46} \\ -\rho_{51} & -\rho_{52} & -2\rho_{53} & -2\rho_{54} & -2\rho_{55} & -2\rho_{56} \\ -\rho_{61} & -\rho_{62} & -2\rho_{63} & -2\rho_{64} & -2\rho_{65} & -2\rho_{66} \end{pmatrix} \quad (\text{A3})$$

describes the radioactive decay of the excited states  $|3\rangle$ ,  $|4\rangle$ ,  $|5\rangle$ , and  $|6\rangle$  characterized by the decay rate  $\Gamma = 1/141$  GHz;  $\alpha$  and  $L$  are the resonant thickness and the length of the medium, respectively. The boundary condition gives the Rabi frequency of the incident x-ray field  $\Omega_R(t, 0) = \Omega_L(t, 0) = e^{-(\Gamma/2)t} \frac{1}{2} [1 + \tanh[4(t/\tau)]]$ , where the exponential decay depicts the radioactive decay from excited  $^{57}\text{Fe}$  nuclei, and the hyperbolic tangent simulates the time gating with  $\tau = 5$  ns. Moreover,  $\Omega_H(t, 0) = 0$  for the forward emission. The used initial conditions are based on facts that initially X-ray field is absent, ground states  $|1\rangle$  and  $|2\rangle$  are equally and only populated and no coherence is built in advance, namely,  $\rho_{11}(0, y) = \rho_{22}(0, y) = 1/2$ ,  $\rho_{ii}(0, y) = 0$  for  $i > 2$  and  $\rho_{ij}(0, y) = 0$  for  $i \neq j$ .

## APPENDIX B: OPTICAL BLOCH EQUATION FOR THE CASE OF A SWITCHED MAGNETIC FIELD

For general cases of continuous and relatively slow magnetic switching, it is convenient to fix the quantization axis along the  $z$  axis and then rotate  $\hat{H}_h$  at each  $\theta$  back onto the  $z$  axis. We now derive the rotated master equation of the density matrix. The Schrödinger equations along the switched magnetic field are  $i\hbar(\partial/\partial t)|\psi\rangle = \hat{H}|\psi\rangle$  and  $-i\hbar(\partial/\partial t)\langle\psi| = \langle\psi|\hat{H}^\dagger$ . The associated master equation is then given by

$$\frac{\partial}{\partial t}(|\psi\rangle\langle\psi|) = \left(\frac{\partial}{\partial t}|\psi\rangle\right)\langle\psi| + |\psi\rangle\left(\frac{\partial}{\partial t}\langle\psi|\right).$$

By substituting the Schrödinger equation on the right-hand side, one obtains

$$\frac{\partial}{\partial t}(|\psi\rangle\langle\psi|) = \frac{1}{i\hbar}(\hat{H}|\psi\rangle)\langle\psi| - \frac{1}{i\hbar}|\psi\rangle(\langle\psi|\hat{H}^\dagger),$$

which then becomes the typical master equation  $\partial_t \hat{\rho} = (1/i\hbar)[\hat{H}, \hat{\rho}]$ . The same derivation procedure can apply to the rotating case using the rotation operator  $\hat{R} = e^{-i(\hat{J}/\hbar)\cdot\hat{n}\theta(t)}$ , where  $\hat{J}$  is the angular momentum operator,  $\hat{n}$  is the rotation axis, and  $\theta(t)$  is the time-dependent switching angle between the  $z$  axis and the magnetic field at some moment  $t$ . Along the  $z$  axis as the fixed quantization axis,

we have

$$\begin{aligned} \frac{\partial}{\partial t}(\hat{R}|\psi\rangle\langle\psi|\hat{R}^\dagger) &= \hat{R}\left(\frac{\partial}{\partial t}|\psi\rangle\right)\langle\psi|\hat{R}^\dagger + \hat{R}|\psi\rangle\left(\frac{\partial}{\partial t}\langle\psi|\right)\hat{R}^\dagger \\ &\quad + \left(\frac{\partial}{\partial t}\hat{R}\right)|\psi\rangle\langle\psi|\hat{R}^\dagger + \hat{R}|\psi\rangle\langle\psi|\left(\frac{\partial}{\partial t}\hat{R}^\dagger\right) \\ &= \frac{1}{i\hbar}\hat{R}\hat{H}\hat{R}^\dagger\hat{R}|\psi\rangle\langle\psi|\hat{R}^\dagger \\ &\quad - \frac{1}{i\hbar}\hat{R}|\psi\rangle\langle\psi|\hat{R}^\dagger\hat{H}\hat{R}^\dagger \\ &\quad + \left(\frac{\partial}{\partial t}\hat{R}\right)|\psi\rangle\langle\psi|\hat{R}^\dagger + \hat{R}|\psi\rangle\langle\psi|\left(\frac{\partial}{\partial t}\hat{R}^\dagger\right). \end{aligned}$$

When the magnetic field is switched continuously, the  $\hat{R}$  is time dependent, and the master equation turns into

$$\begin{aligned} \partial_t \hat{\rho}^z &= \frac{1}{i\hbar}[\hat{H}^z, \hat{\rho}^z] - i\frac{\hat{J}}{\hbar} \cdot \hat{n} \frac{\partial\theta}{\partial t} \hat{R}|\psi\rangle \\ &\quad \times \langle\psi|\hat{R}^\dagger + \frac{\partial\theta}{\partial t} \hat{R}|\psi\rangle\langle\psi|\hat{R}^\dagger i\frac{\hat{J}}{\hbar} \cdot \hat{n} \\ &= \frac{1}{i\hbar}[\hat{H}^z, \hat{\rho}^z] + \frac{\hat{J} \cdot \hat{n}}{i\hbar} \frac{\partial\theta}{\partial t} \hat{\rho}^z - \frac{\partial\theta}{\partial t} \hat{\rho}^z i\frac{\hat{J}}{\hbar} \cdot \hat{n} \\ &= \frac{1}{i\hbar} \left[ \hat{H}^z + \frac{\partial\theta}{\partial t} \hat{J} \cdot \hat{n}, \hat{\rho}^z \right]. \end{aligned}$$

For simplicity, we remove the  $z$  index of  $\hat{\rho}^z$ , and the OBE of a time-dependent rotating system then becomes

$$\begin{aligned} \partial_t \hat{\rho} &= \frac{1}{i\hbar}[\hat{H}, \hat{\rho}] + \mathcal{L}\rho, \\ \hat{H} &= \hat{H}_i + \hat{H}_h^z + \frac{\partial\theta}{\partial t} \hat{J}_y, \end{aligned} \tag{B1}$$

where  $\hat{J}_y$  is the  $y$  component of the angular momentum operator when the magnetic field is switched about the  $y$  axis [43]. The  $\theta$ -independent  $\hat{H}_i$  show the convenience of the scheme, such that one can always use the same definition of the x-ray polarizations. The rotated hyperfine Hamiltonian reads as follows:

$$\hat{H}_h^z = \hat{R}(-\theta)\hat{H}_h\hat{R}^\dagger(-\theta) = \begin{pmatrix} -\delta_g \cos \theta(t) & -\delta_g \sin \theta(t) & 0 & 0 & 0 & 0 \\ -\delta_g \sin \theta(t) & \delta_g \cos \theta(t) & 0 & 0 & 0 & 0 \\ 0 & 0 & 3\delta_e \cos \theta(t) & \sqrt{3}\delta_e \sin \theta(t) & 0 & 0 \\ 0 & 0 & \sqrt{3}\delta_e \sin \theta(t) & \delta_e \cos \theta(t) & 2\delta_e \sin \theta(t) & 0 \\ 0 & 0 & 0 & 2\delta_e \sin \theta(t) & -\delta_e \cos \theta(t) & \sqrt{3}\delta_e \sin \theta(t) \\ 0 & 0 & 0 & 0 & \sqrt{3}\delta_e \sin \theta(t) & -3\delta_e \cos \theta(t) \end{pmatrix},$$



where  $\hat{R}(-\theta)$  is the rotation operator [43].

Due to the weak x-ray intensity of the  $^{57}\text{Co}$  source, in both cases we work in the perturbation regime, namely,  $|\Omega_R| \ll \Gamma$ ,  $|\Omega_H| \ll \Gamma$ , and  $|\Omega_L| \ll \Gamma$ , such that only terms of  $\rho_{i1}$  and  $\rho_{j2}$ , where  $i > 2$  and  $j > 2$ , are used in the calculations.  $\alpha = 30$ ,  $\delta_g = 12.63\Gamma$  and  $\delta_e = 7.37\Gamma$  are used for all figures in the main text.

Because the x-ray propagation time, namely,  $L/c$ , is of the order of 0.1 ps, which is much shorter than the nanosecond time scale of interest, this allows for the typical procedure to neglect the temporal derivative terms in the wave equations. The OBE can then be numerically solved by the Runge-Kutta fourth-order method (RK4) [42], with  $L = 10 \mu\text{m}$ , and grid spacings  $\Delta y = 0.1 \mu\text{m}$  and  $\Delta t = 3 \times 10^{-3} \text{ ns}$ . All solutions have been double checked using the `NDSolve` function of Mathematica 11 for the complete ODE, including the temporal derivative terms in the wave equations. No significant deviation has been observed, which confirms the convergence of the solution.

- 
- [1] B. W. Adams, C. Buth, S. M. Cavaletto, J. Evers, Z. Harman, C. H. Keitel, A. Pálffy, A. Picón, R. Röhlsberger, Y. Rostovtsev, and K. Tamasaku, x-ray quantum optics, *J. Mod. Opt.* **60**, 2 (2013).
- [2] Y. V. Shvyd'ko, T. Hertrich, U. van Bürck, E. Gerdau, O. Leupold, J. Metge, H. D. Rüter, S. Schwendy, G. V. Smirnov, W. Potzel, and P. Schindermann, Storage of Nuclear Excitation Energy Through Magnetic Switching, *Phys. Rev. Lett.* **77**, 3232 (1996).
- [3] C. Buth, R. Santra, and L. Young, Electromagnetically Induced Transparency for X-rays, *Phys. Rev. Lett.* **98**, 253001 (2007).
- [4] K. Tamasaku and T. Ishikawa, Interference Between Compton Scattering and X-Ray Parametric Down-Conversion, *Phys. Rev. Lett.* **98**, 244801 (2007).
- [5] T. Glover, M. Hertlein, S. Southworth, T. Allison, J. Van Tilborg, E. Kanter, B. Krässig, H. Varma, B. Rude, R. Santra, A. Belkacem, and L. Young, Controlling x rays with light, *Nat. Phys.* **6**, 69 (2010).
- [6] R. Röhlsberger, K. Schlage, B. Sahoo, S. Couet, and R. Ruffer, Collective Lamb shift in single-photon superradiance, *Science* **328**, 1248 (2010).
- [7] N. Rohringer, D. Ryan, R. A. London, M. Purvis, F. Albert, J. Dunn, J. D. Bozek, C. Bostedt, A. Graf, R. Hill, S. P. Hau-Riege, and J. J. Rocca, Atomic inner-shell x-ray laser at 1.46 nanometres pumped by an x-ray free-electron laser, *Nature* **481**, 488 (2012).
- [8] R. Röhlsberger, H. C. Wille, K. Schlage, and B. Sahoo, Electromagnetically induced transparency with resonant nuclei in a cavity, *Nature* **482**, 199 (2012).
- [9] T. E. Glover, D. M. Fritz, M. Cammarata, T. K. Allison, S. Coh, J. M. Feldkamp, H. Lemke, D. Zhu, Y. Feng, R. N. Coffee, M. Fuchs, S. Ghimire, J. Chen, S. Schwartz, D. A. Reis, S. E. Harris, and J. B. Hastings, X-ray and optical wave mixing, *Nature* **488**, 603 (2012).
- [10] S. Schwartz, R. N. Coffee, J. M. Feldkamp, Y. Feng, J. B. Hastings, G. Y. Yin, and S. E. Harris, X-Ray Parametric Down-Conversion in the Langevin Regime, *Phys. Rev. Lett.* **109**, 013602 (2012).
- [11] K. P. Heeg, H.-C. Wille, K. Schlage, T. Guryeva, D. Schumacher, I. Uschmann, K. S. Schulze, B. Marx, T. Kämpfer, G. G. Paulus, R. Röhlsberger, and J. Evers, Vacuum-Assisted Generation and Control of Atomic Coherences at X-Ray Energies, *Phys. Rev. Lett.* **111**, 073601 (2013).
- [12] K. P. Heeg, J. Haber, D. Schumacher, L. Bocklage, H.-C. Wille, K. S. Schulze, R. Loetzsch, I. Uschmann, G. G. Paulus, R. Ruffer, R. Röhlsberger, and J. Evers, Tunable Subluminal Propagation of Narrow-Band X-Ray Pulses, *Phys. Rev. Lett.* **114**, 203601 (2015).
- [13] K. P. Heeg, C. Ott, D. Schumacher, H.-C. Wille, R. Röhlsberger, T. Pfeifer, and J. Evers, Interferometric Phase Detection at X-Ray Energies via Fano Resonance Control, *Phys. Rev. Lett.* **114**, 207401 (2015).
- [14] K. P. Heeg, A. Kaldun, C. Strohm, P. Reiser, C. Ott, R. Subramanian, D. Lentrodt, J. Haber, H.-C. Wille, S. Goertler, R. Ruffer, C. H. Keitel, R. Röhlsberger, T. Pfeifer, and J. Evers, Spectral narrowing of x-ray pulses for precision spectroscopy with nuclear resonances, *Science* **357**, 375 (2017).
- [15] T. J. Bürvenich, J. Evers, and C. H. Keitel, Nuclear Quantum Optics with X-Ray Laser Pulses, *Phys. Rev. Lett.* **96**, 142501 (2006).
- [16] A. Pálffy, C. H. Keitel, and J. Evers, Single-Photon Entanglement in the keV Regime via Coherent Control of Nuclear Forward Scattering, *Phys. Rev. Lett.* **103**, 017401 (2009).
- [17] S. Schwartz and S. E. Harris, Polarization Entangled Photons at X-Ray Energies, *Phys. Rev. Lett.* **106**, 080501 (2011).
- [18] W.-T. Liao, A. Pálffy, and C. H. Keitel, Nuclear coherent population transfer with x-ray laser pulses, *Phys. Lett. B* **705**, 134 (2011).
- [19] W.-T. Liao, A. Pálffy, and C. H. Keitel, Coherent Storage and Phase Modulation of Single Hard-x-Ray Photons Using Nuclear Excitons, *Phys. Rev. Lett.* **109**, 197403 (2012).
- [20] W.-T. Liao, A. Pálffy, and C. H. Keitel, Three-beam setup for coherently controlling nuclear-state population, *Phys. Rev. C* **87**, 054609 (2013).
- [21] W.-T. Liao and A. Pálffy, Proposed Entanglement of X-Ray Nuclear Polaritons as a Potential Method for Probing Matter at the Subatomic Scale, *Phys. Rev. Lett.* **112**, 057401 (2014).
- [22] W.-T. Liao, C. H. Keitel, and A. Pálffy, x-ray-generated heralded macroscopical quantum entanglement of two nuclear ensembles, *Sci. Rep.* **6**, 33361 (2016).
- [23] X. Kong and A. Pálffy, Stopping Narrow-Band X-Ray Pulses in Nuclear Media, *Phys. Rev. Lett.* **116**, 197402 (2016).
- [24] S. M. Cavaletto, Z. Harman, C. Ott, C. Buth, T. Pfeifer, and C. H. Keitel, Broadband high-resolution x-ray frequency combs, *Nat. Photonics* **8**, 520 (2014).
- [25] J. Gunst, C. H. Keitel, and A. Pálffy, Logical operations with single x-ray photons via dynamically-controlled nuclear resonances, *Sci. Rep.* **6**, 25136 (2016).

- [26] J. Gunst and A. Pálffy, x-ray quantum-eraser setup for time-energy complementarity, *Phys. Rev. A* **94**, 063849 (2016).
- [27] O. Kocharovskaya, R. Kolesov, and Y. Rostovtsev, Coherent Optical Control of Mössbauer Spectra, *Phys. Rev. Lett.* **82**, 3593 (1999).
- [28] W.-T. Liao and A. Pálffy, Optomechanically induced transparency of x-rays via optical control, *Scientific Reports* **7**, 321 (2017).
- [29] R. Röhlberger, *Nuclear Condensed Matter Physics with Synchrotron Radiation: Basic Principles, Methodology and Applications* (Springer-Verlag, Heidelberg, 2004).
- [30] G. K. Shenoy, in *NASSAU 2006* (Springer-Verlag, Heidelberg, 2007), p. 5.
- [31] F. Vagizov, V. Antonov, Y. Radeonychev, R. N. Shakhmuratov, and O. Kocharovskaya, Coherent control of the waveforms of recoilless  $\gamma$ -ray photons, *Nature* **508**, 80 (2014).
- [32] G. V. Smirnov, Y. V. Shvyd'ko, O. S. Kolotov, V. A. Pogozhev, M. Kotrbova, S. Kadechkova, and I. Novak, Nanosecond modulation of  $\text{Fe}^{57}$  Mössbauer radiation, *Sov. Phys. JETP* **59**, 875 (1984).
- [33] Y. V. Shvyd'ko, S. Popov, and G. Smirnov, Coherent re-emission of gamma-quanta in the forward direction after a stepwise change of the energy of nuclear excitation, *J. Phys. Condens. Matter* **5**, 1557 (1993).
- [34] W.-T. Liao and S. Ahrens, Gravitational and relativistic deflection of x-ray superradiance, *Nat. Photonics* **9**, 169 (2015).
- [35] G. V. Smirnov, Y. V. Shvyd'ko, and E. Realo, Accelerated decay of nuclear excitation in a crystal during resonant gamma quanta scattering, *JETP Lett.* **39**, 41 (1984).
- [36] Y. V. Shvyd'ko, G. V. Smirnov, S. L. Popov, and T. Hertrich, Observation of intensified forward gamma-ray emission in spontaneous nuclear decay, *JETP Lett.* **53**, 69 (1991).
- [37] K. Szymański, Polarized radiation in Mössbauer spectroscopy, *Phys. Rep.* **423**, 295 (2006).
- [38] O. Kolotov, A. Krasnojon, and V. Pogozhev, On the intensity of shock-initiated magnetoelastic oscillations arising in iron borate single crystals during pulsed magnetizing or magnetization-switching processes, *Tech. Phys.* **43**, 1126 (1998).
- [39] D. Afanasiev, I. Razdolski, K. M. Skibinsky, D. Bolotin, S. V. Yagupov, M. B. Strugatsky, A. Kirilyuk, T. Rasing, and A. V. Kimel, Laser Excitation of Lattice-Driven Anharmonic Magnetization Dynamics in Dielectric  $\text{FeBO}_3$ , *Phys. Rev. Lett.* **112**, 147403 (2014).
- [40] A. Pálffy and J. Evers, Coherent control of nuclear forward scattering, *J. Mod. Opt.* **57**, 1993 (2010).
- [41] M. O. Scully and M. S. Zubairy, *Quantum Optics* (Cambridge University Press, Cambridge, 2006).
- [42] W. H. Press, S. A. Teukolsky, W. T. Vetterling, and B. P. Flannery, *Numerical Recipes in C* (Cambridge University Press, Cambridge, 1996).
- [43] J. J. Sakurai, *Modern Quantum Mechanics* (Addison-Wesley, Boston, 1994).
- [44] Y. V. Shvyd'ko, Nuclear resonant forward scattering of x rays: Time and space picture, *Phys. Rev. B* **59**, 9132 (1999).
- [45] Y. V. Shvyd'ko and U. Van Bürck, Hybrid forms of beat phenomena in nuclear forward scattering of synchrotron radiation, *Hyperfine Interact.* **123**, 511 (1999).
- [46] G. K. Shenoy, Scientific legacy of Stanley Ruby, *Hyperfine Interact.* **170**, 5 (2006).
- [47] J. B. Hastings, D. P. Siddons, U. van Bürck, R. Hollatz, and U. Bergmann, Mössbauer Spectroscopy using Synchrotron Radiation, *Phys. Rev. Lett.* **66**, 770 (1991).
- [48] U. van Bürck, D. P. Siddons, J. B. Hastings, U. Bergmann, and R. Hollatz, Nuclear forward scattering of synchrotron radiation, *Phys. Rev. B* **46**, 6207 (1992).